SUPPLEMENTARY INFORMATION

Methane Photolysis to Clean Hydrogen and Carbon Nanotubes

Abdelaziz Gouda[*1,2,3] Juan Manuel Restrepo-Flórez[4], Abhinav Mohan[1,2,3], Otavio Augusto Titton Dias[3], Andrew Wang[1], Camilo J. Viasus Perez[1,5], Jessica Ye[1,3], Tamlyn Slocombe[1], Vijay K. Tomer[3], Jiabao Shen[6], Nhat Truong Nguyen[7], Nazir Kherani[6], Mohamad Hmadeh[1,8], Alán Aspuru-Guzik[1,2,9], Mohini Sain[*2,3] and Geoffrey Ozin[*1,2]

[1] Department of Chemistry, University of Toronto, 80 Saint George St., Toronto, Ontario M5S 3H6, Canada

[2]Department of Applied Chemistry and Chemical Engineering, University of Toronto, 200 College St., Toronto, ON M5S 3E5, Canada

[3]Department of Mechanical and Industrial Engineering, University of Toronto, 5 King's College Rd, Toronto, ON, M5S 3G8, Canada

[4]Department of Chemical Engineering, University of Florida, Gainesville, Florida 32611, United States

[5]Grupo de Investigación en Química de Coordinación y Bioinorgánica, Departamento de Química, Facultad de Ciencias, Universidad Nacional de Colombia, Av. Carrera 30 # 45-03, Sede Bogotá, Colombia

[6]Department of Electrical and Computing Engineering, University of Toronto, 10 King's College Road, Toronto, Ontario M5S 3G4, Canada

[7]Department of Chemical and Materials Engineering, Gina Cody School of Engineering and Computer Science, Concordia University, Montreal, Quebec, Canada

[8]Department of Chemistry, Faculty of Arts and Sciences, American University of Beirut, P.O. Box 11-0236, Beirut 1107 2020, Lebanon

[9]Department of Computer Science, University of Toronto, Sandford Fleming Building, 10 King's College Road, Toronto, Ontario M5S 3G4, Canada

Materials and Methods

Materials: Ni/alumina, Ni/SiO_2, and Ni/MgO were purchased from Riogen (Catalysis for Chemicals & Energy) and used as received. Multiwalled Carbon nanotubes (CNT), Nickel (II) nitrate hexahydrate, Gamma Alumina oxide, and Nickel powder were purchased from Sigma-Aldrich and used as received. Before use, methane (99.97% purity) and argon (99.9% purity) were purchased from Praxair and were passed through a dry alumina column. For the photocatalytic tests, catalyst pellets of about 100-135 mg made with an average diameter of 13 mm between 2-3 mm thickness were prepared using a commercial pellet press at 2 metric tonnes for 5 minutes.

Thermogravimetric Analysis: TGA experiments were performed on a Discovery Series TGA from TA Instruments. A constant gas flow of 10 mL/min was used for a single-step ramp under 5% O_2/N_2 over fresh and spent catalysts. The temperature was ramped from 100 to 900 ºC at 5 ºC /min.

Characterization: PXRD patterns were collected on a Bruker D2-Phaser X-ray diffractometer using Cu Kα radiation at 30 kV. Diffuse reflectance spectra were collected using a Lambda 1050 UV/vis/NIR PerkinElmer spectrometer with an integrating sphere. XPS of as received and post-reaction samples were performed on a Thermo Scientific Kα with an Al Kα X-ray source. SEM and TEM were done using a Hitachi S-5200 HRSEM and JEOL 2010 HRTEM, respectively. The average length of the carbon nanotubes was determined through image analysis of SEM and TEM micrographs using ImageJ software. Despite the bent and entangled ("spaghetti-like") morphology, individual nanotube segments were manually traced and measured across multiple images to obtain a statistically representative average length. BET measurement was recorded by an accelerated surface area and porosimetry analyzer (Micromeritics ASAP 2020) with N_2 adsorption analysis. Raman measurements were performed using a Renishaw InVia Raman microscope equipped with a CCD detector and internal silicon calibration (520.5 cm^{-1}). Spectra were acquired with a 20× objective, 10 s exposure time, and three accumulations per scan, applying arPLS baseline correction. Fixed polarization was used. Two excitation wavelengths of 638 and 785 nm were employed.

The surface temperature of the catalyst was measured using an IR camera that was calibrated to obtain an accurate emissivity value for the catalyst, and the calibration details are: The calibration steps for the FLIR EX320 thermal camera included:

First, determine the reflected temperature of the sample by placing a pre-crumpled aluminum foil (emissivity =1), above the catalyst sample at room temperature and noting the temperature reading from the thermal camera to set as the reflected temperature.

Second, place a reference blackbody on the catalyst sample, in this work a small square piece of electrical insulation tape, (with a thin 1mm k-type thermocouple wedged between the catalyst sample and tape to cross-validate the temperature). The emissivity of the catalyst sample is changed till it matches the temperature reading of the tape with an emissivity set to 0.98 in the camera, at an elevated temperature of 100°C used. The temperature was measured at a fixed distance of 15 cm from the sample holder, with a lens with a focal length of 27.4 mm and focus and temperature range adjusted at 4x magnification.

Catalytic tests: The catalytic tests were performed in horizontal, vertical, fixed-bed reactors as illustrated below. Pellets of 13 mm diameter were placed in a reactor equipped with a quartz window and irradiated with a 300W Xe arc lamp from Perfect Light company was used in the power and wavelength experiments. All measurements were conducted by a flame ionization detector (FID) and Thermal conductivity detector (TCD) on an SRI8610 GC instrument. Thermal tests were performed in the same horizontal fixed-bed reactor. The temperature of the particles was accurately measured using a thermocouple that was carefully placed below the catalyst. A homemade electrical heating system is installed at the base of the reactor, providing the thermal energy required for thermal reactions. The temperature of the electrical heating system was also measured by a thermocouple. An OMEGA temperature controller was configured to regulate the temperature of particles or the reactor. This setup allowed for precise readings of the thermal properties of the particles, ensuring that the measurement reflected the actual temperature of the material in situ.

Kinetic experiments: Kinetic experiments were performed where the Xe arc lamp light intensity was set to 10.6 W cm^{-2} and the reactor pressure was set to 14.6 psi in each run. The reactivity of the methane photolysis may be evaluated using the time expression represented in Equation (1).

$$t = Ao \int_{fA1}^{fA2} \frac{dfA}{(rA)SA} \qquad (1)$$

Where Ao is the initial moles of CH_4, rA is the CH_4 reaction rate, SA is the exposed surface area to light, and fA1 and fA2 are the fractions of the remaining CH_4 reactant concentration as the reaction proceeds.

From the first-rate law.

$$rA = k\,[A] \tag{2}$$

Where k is the reaction constant and [A] is the CH_4 concentration over time, the reaction order (n = 0.041) for the methane photolysis reaction is shown in equation (3).

$$\ln(rA) = \ln k + n \ln(A) \tag{3}$$

From equation (2), [A] can be replaced with the mole fraction expression

$$fA = \frac{Ao-[A]}{Ao} \tag{4}$$

to produce (5)

$$rA = k\,(Ao)\,(1 - fA) \tag{5}$$

Once we replace (5) in (1) and integrate over the reaction fraction fA1 and fA2, we obtain the reaction constant k for each reaction time as presented in (6)

$$k = \frac{1}{.SA.t}(-ln(1 - fA)) \tag{6}$$

As a result, k =0.446±0.105 h^{-1} was calculated from each time step, and the stoichiometry of the reaction produced 2x rA, which represents the H_2 rate, is calculated as 6.98±1.71 mmol cm^{-2} h^{-1}.

Optothermal modeling

To compare and validate the temperature distribution of the catalyst sample pellet experimentally obtained from the thermocouple, a finite element model heat transfer model was implemented in COMSOL Multiphysics, considering a fluid phase of mixed gases of 1:1 ratio of methane to argon (with a velocity of 0.052 m/s) and solid phases of the reactor holder and body. An effective thermal conductivity was assumed for the catalyst using the Maxwell Garnett effective medium approximation[1-3] (expression for effective thermal conductivity shown in (7)) comparable with

empirically obtained effective thermal conductivity for Ni/Al_2O_3 catalyst pellet in literature[4]. (where f_v is the volume fraction of the oxide in the composite). A 2D-axisymmetric model comprising of the catalyst, stainless steel reactor and the gas was created. The10wt% Ni loading of the catalyst corresponds to a very large number of nickel particles in the sample ($>10^{14}$), for which local heating effects are negligible (The delta Temperature increase of the single Ni nanoparticle compared to the collective heating of the ensemble of nanoparticles is negligible) and collective heating dominates[5, 6]. Therefore, different deposited beam powers were input for a Gaussian beam with a standard deviation of 5 mm as the source term for collective heating. The deposited beam power accounts for the ~92% average fractional absorption (as measured from UV-VIS reflectance measurement (Fig. S8a) by the catalyst sample and ~92% transmission through the quartz glass window. Conduction and convective fluxes (at the boundaries of the support and reactor surface) were considered as the heat loss terms at steady state, with the temperature of the external reactor walls set from 25-40°C as monitored with a thermocouple for the different irradiances.

$$\kappa_{h,eff} = k_{air} + \frac{\frac{3f_v\kappa_{air}}{\kappa_{Al_2O_3} + 2\kappa_{air}}}{\kappa_{Al_2O_3} - \kappa_{air}} - f_v \qquad (7)$$

Density Functional Theory (DFT) calculations

We performed spin-polarized DFT calculations using the Vienna Ab-initio Simulation Package (VASP)[7-10] with projected augmented wave (PAW) pseudopotentials[11] (for all elements, we used the "GW" versions of the pseudopotentials with the extensions "_sv" (i.e. the *s* and *p* semi-core states are treated as valence states). All calculations have a plane-wave basis cutoff of 600 eV. For all structural relaxations, we employed the r^2SCAN functional with the rVV10 van der Waals correction[12, 13]. The surface model was constructed by first relaxing bulk γ-Al_2O_3 from the model of Digne *et al.*[14] (with the cif file provided by Peterson[14] using a 4 x 4 x 4 k-point mesh, with convergence criteria of forces and the electronic self-consistent (SCF) loop set to 0.01 eV/Å and 10^{-7} eV, respectively. This yielded cell parameters a= 5.503 Å, b = 8.276 Å, 7.970 Å, and β = 90.69°, in good agreement with previous reports[14, 15]. Using the relaxed bulk structure, we then

constructed the (100) surface of Al_2O_3 with approximately 16.5 Å of vacuum space in the c-direction, using the cif2cell Python package[16]. From the relaxed Al_2O_3(100) surface we then added, to the surface, a cluster of 7 Ni atoms in a (111) pattern and re-relaxed the structure. For all surface relaxations, we kept the cell parameters fixed while allowing the atoms in the top half of the slab to move (the bottom half were fixed at the bulk positions), sampled the Brillouin zone at the Γ point, employed force and electronic SCF criteria of 0.03 eV/Å and 10^{-5} eV (respectively), and included dipole corrections along the c-axis.

To simulate excited state processes, we employed the TD-DFT approach within VASP[17-19]. We used the geometries obtained with r^{2}SCAN+rVV10, and first calculated the ground state electronic structure at the HSE06 (ω = 0.2)[20] level with dipole and dispersion corrections included, at the Γ point, and electronic SCF convergence at 10^{-5} eV. We employed dispersion corrections at the DFT-D3(BJ) level[21, 22], with the parameters for Becke-Johnson damping selected based on those of the PBE0, as was done by ref. [23]. The ground state HSE wavefunction then served as the input to calculate the frequency-dependent dielectric matrix using a total of 1600 bands (approximately 55% unoccupied), the result of which was then used to evaluate the Casida equation under the Tamm-Dancoff Approximation. For the latter, we used 20 occupied and unoccupied frontier bands to obtain the imaginary dielectric function (simulating the absorption coefficient) and the oscillator strengths (simulating the probability of individual transitions).

We then selected excitations with an oscillator strength greater than 0.1 and between 0 and 4 eV for plotting and further analysis. Within linear response TDDFT and in the outputs given by VASP, each oscillator strength that gets printed corresponds to a linear combination of all possible 1-electron interband transitions within the number of occupied and unoccupied bands specified – often, a few of these transitions contribute a lot and most do not contribute much (on the other hand, an individual transition can also contribute to multiple excitations across several wavelengths). The contribution of an individual transition from an occupied band/orbital i to an unoccupied band/orbital j is given by the interband coupling constant X_{ij} for that pair of orbitals, which essentially describes how much a specific orbital orbital pair contributes to a certain excitation. For each selected excitation, we visualized the 1-electron interband transitions for origin and destination bands/orbitals with $X_{ij} > 0.1$ and plotted the differences between the partial charge densities of the destination and origin orbitals (i.e. destination orbital minus origin orbital).

Charge density differences between the relevant bands were generated using VASPKIT[24] and visualized with VESTA[25] at an isosurface level of 0.001 e $Bohr^{-3}$ unless otherwise indicated.

MWCNT as anode for Li-ion battery:

Slurry preparation:

The MWCNT slurry consisted of 80 wt% active materials (AM, Photo-grown MWCNT), 10 wt% conducting carbon (CC, Super C45), and a 10 wt% PVDF binder in N-Methyl-2-Pyrrolidone **(**NMP). Slurry preparation involved ball-milling 4 g of AM with 0.5 g of CC for 30 minutes at 500 rpm. Simultaneously, 0.5 g of PVDF was mixed with 5 mL of NMP at 50 °C until a transparent thick viscous solution formed. The pre-mixed AM/CC was then gradually added to this solution in batches to create a uniform slurry, which was stirred continuously at 40 °C for 3 hours. The slurry underwent homogenization using a dual-shaft planetary mixer under vacuum for 30 minutes to eliminate trapped air bubbles.

Electrode preparation: The electrode preparation process involved coating wet slurry onto Cu foil using a tape casting machine equipped with a 10 cm-long doctor blade. The coating was performed at a low speed of 6 mm/s. Following the coating process, the sheets were dried overnight under vacuum at 60 °C. The dried sheets were then calendared to increase tap density and minimize vulnerable pores. The processed sheets were subsequently cut into 1.2 cm electrodes, achieving an average areal MWCNT loading within the range of ∼2.0 mg cm^{-2}.

Coin cell assembly: The assembly was performed in an argon-filled glove box with H_2O and O_2 levels maintained below 0.1 ppm. Single-sided MWCNT-coated sheets were paired with metallic lithium metal (8 mm in diameter) as the counter electrode. A tri-layer separator (PP/PE/PP) with a thickness of 25 μm (Celgard 2325) was used to separate the electrodes. The electrolyte, comprising 1 M lithium hexafluorophosphate ($LiPF_6$) dissolved in a 3:7 volume ratio mixture of ethylene carbonate (EC) and ethyl methyl carbonate (EMC), was added to the assembly. The assembled coin cells were pressed under an argon atmosphere and subsequently transferred to a vacuum oven for aging at 50 °C for 12 hours.

Electrochemical measurements: Galvanostatic charge/discharge profiles of the fabricated half cells were measured within a cut-off voltage range of 3.0 V. Cyclic voltammetry (CV) and electrochemical impedance spectroscopy (EIS) were performed using an Admiral Instruments Squidstat Plus potentiostat. CV plots encompassed a potential range of 0–3.0 V, employing a scan rate of 0.2 mV s^{-1}. EIS curves were obtained under open circuit potential, in a frequency range of 2 MHz-0.01 Hz, with an excitation potential of 10 mV and 20 points per decade.

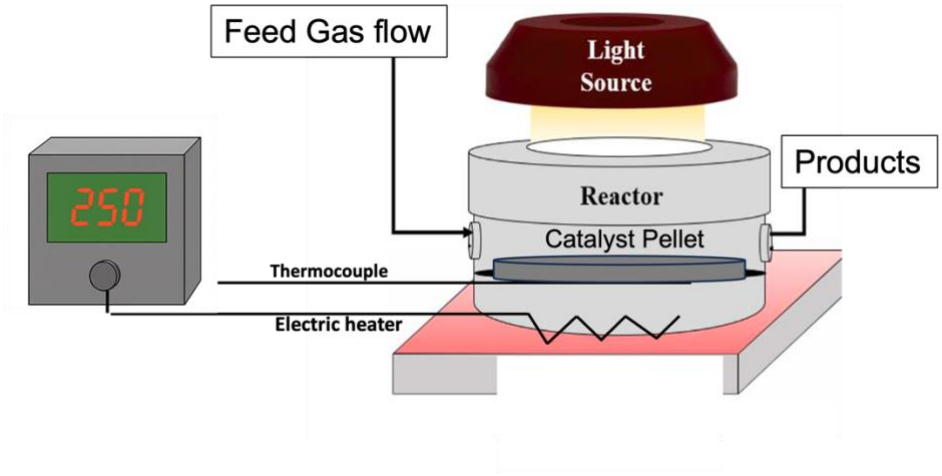

Fig. S1: Schematic representation of the fixed-bed reactor used in this work.

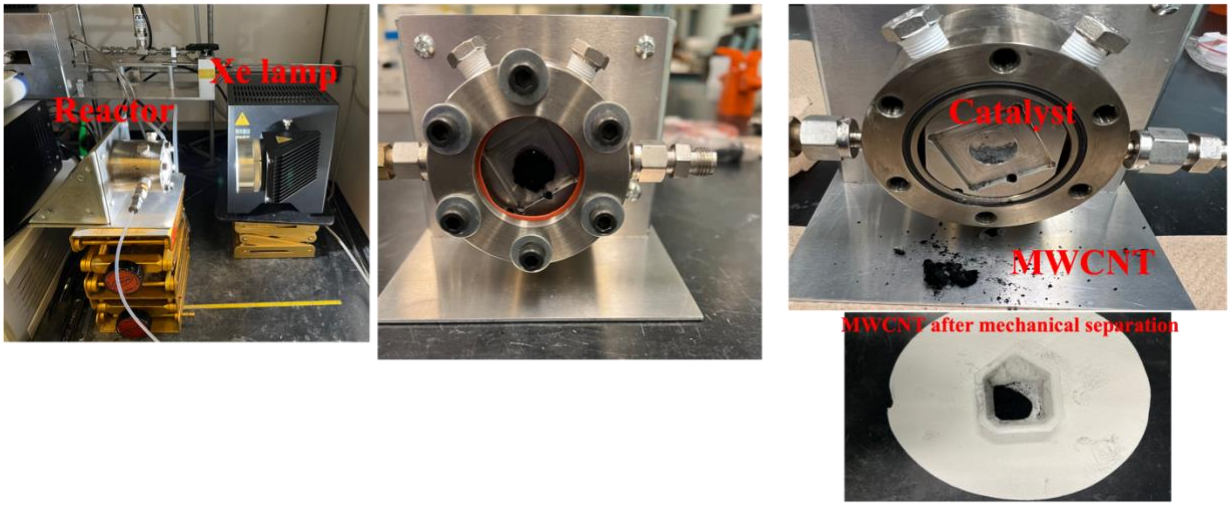

Fig. S2: Vertical fixed-bed reactor used in the methane photolysis process.

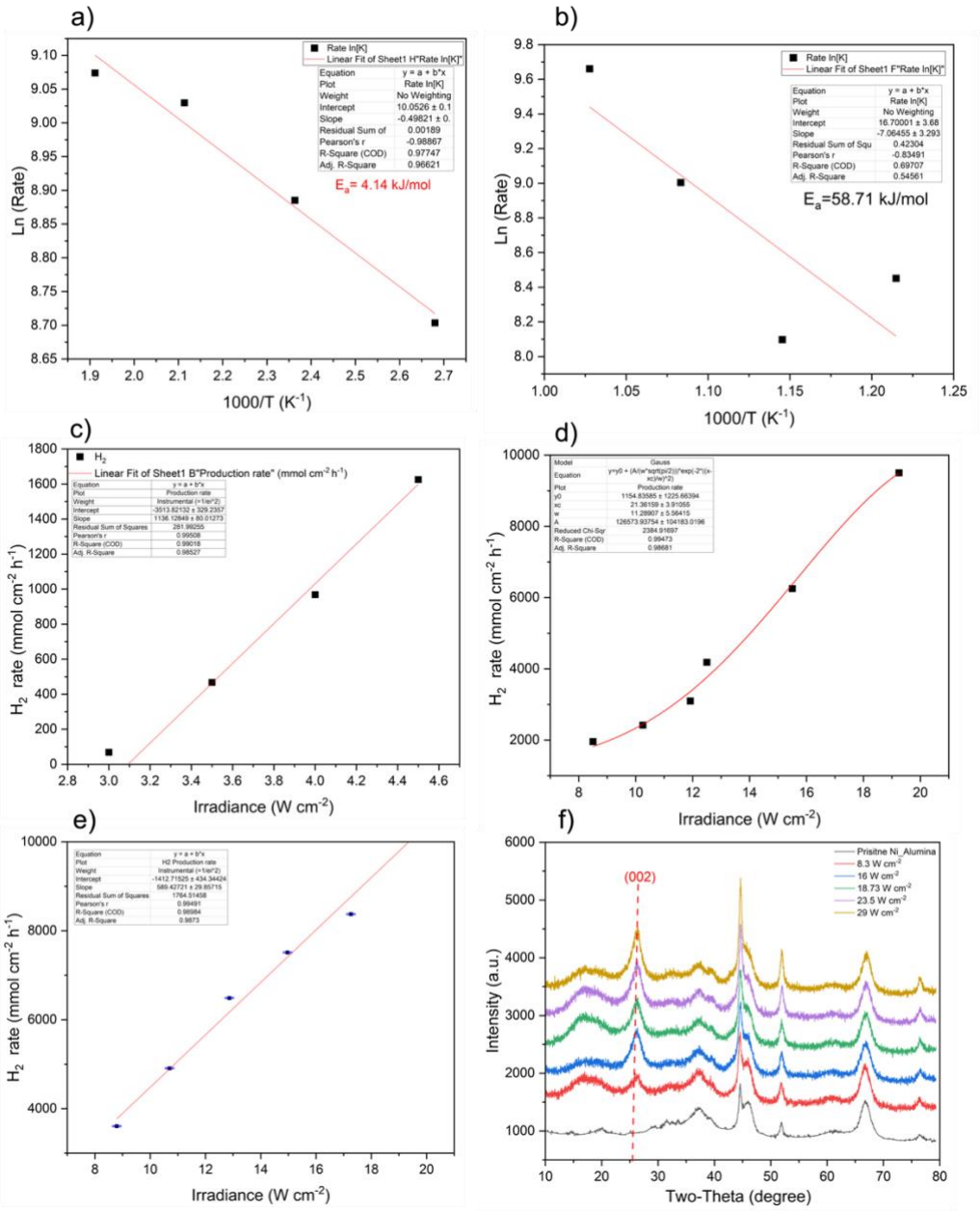

Fig. S3. Methane photolysis performance evaluation: a) Apparent activation energy of the methane photolysis approach over 10% Ni/Al_2O_3 performed at light intensity of 10.6 W cm^{-2}. (b The methane pyrolysis apparent activation energy. c) Linear H_2 rate dependence on the light intensity in the low irradiance regime below 8 W cm^{-2}. d) An Arrhenius trend for H_2 rate dependence on the light intensity in the high irradiance regime above 8 W cm^{-2}. e) linear H_2 rate dependence on the light intensity using 495 nm bandpass filter. f) PXRD patterns of the spent catalyst at different light intensities. In each experiment, the total gas flow was set to 20 sccm (10 sccm CH_4: 10 sccm Ar) with an irradiated sample surface area of 0.785 cm^2. New samples were used for every test condition. At least three individual measurements were used to calculate the error bars.

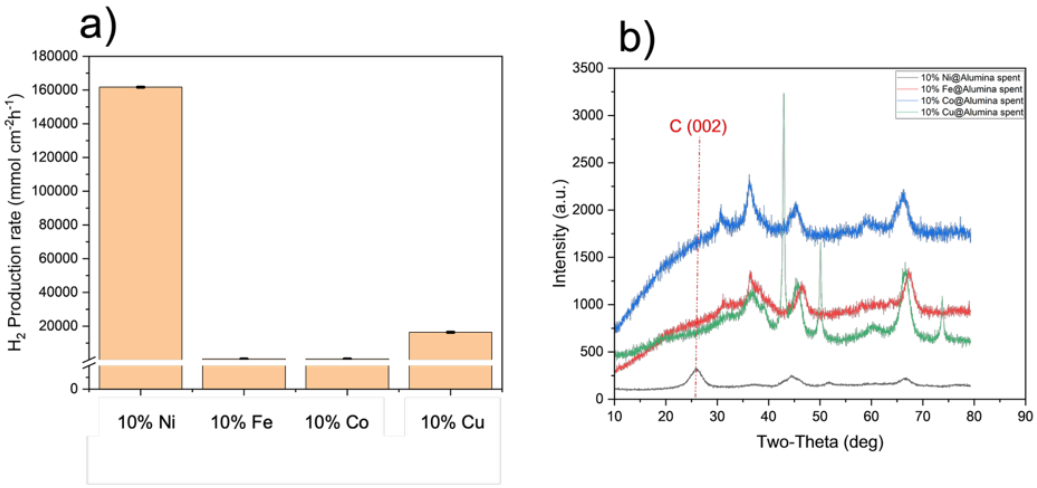

Fig. S4. Methane photolysis performance evaluation over 10% Ni/Al_2O_3, 10% Fe/Al_2O_3, 10% Co/Al_2O_3, and 10% Cu/Al_2O_3 performed at a light intensity of 29 W cm^{-2}. b) PXRD patterns of the spent catalyst. In each experiment, the total gas flow was set to 20 sccm (10 sccm CH4: 10 sccm Ar) with an irradiated sample surface area of 0.785 cm^2. New samples were used for every test condition. At least three individual measurements were used to calculate the error bars.

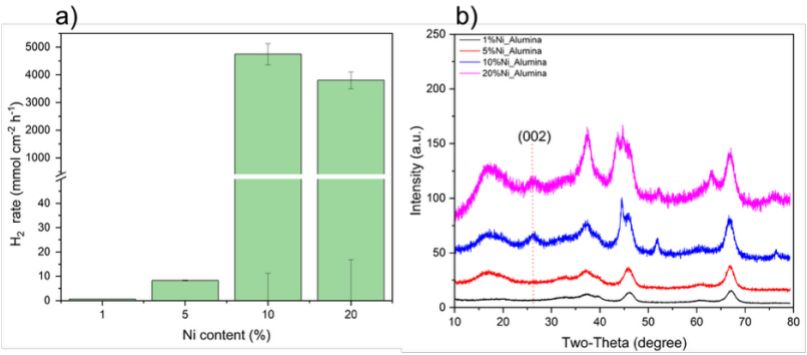

Fig. S5. Methane photolysis performance evaluation over different Ni loadings on Al_2O_3 performed at a light intensity of 10 W cm^{-2}. b) PXRD patterns of the spent catalyst. In each experiment, the total gas flow was set to 20 sccm (10 sccm CH_4: 10 sccm Ar) with an irradiated sample surface area of 0.785 cm^2. New samples were used for every test condition. At least three individual measurements were used to calculate the error bars.

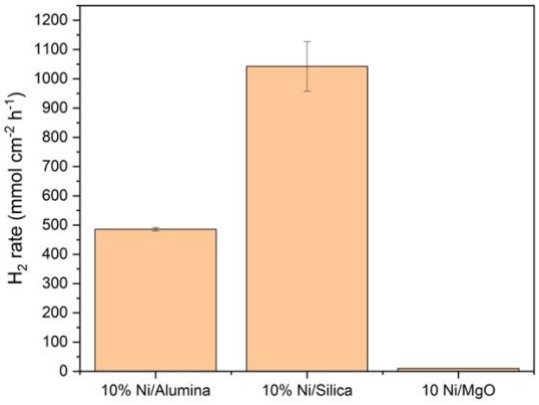

Fig. S6: Comparison of photocatalytic performance for different catalyst supports under identical experimental conditions (5 sccm CH_4 and 5 sccm Ar, irradiated at light intensity of 10.20 W·cm^{-2}), with an irradiated sample surface area of 0.785 cm^2. New samples were used for every test condition. At least three individual measurements were used to calculate the error bars.

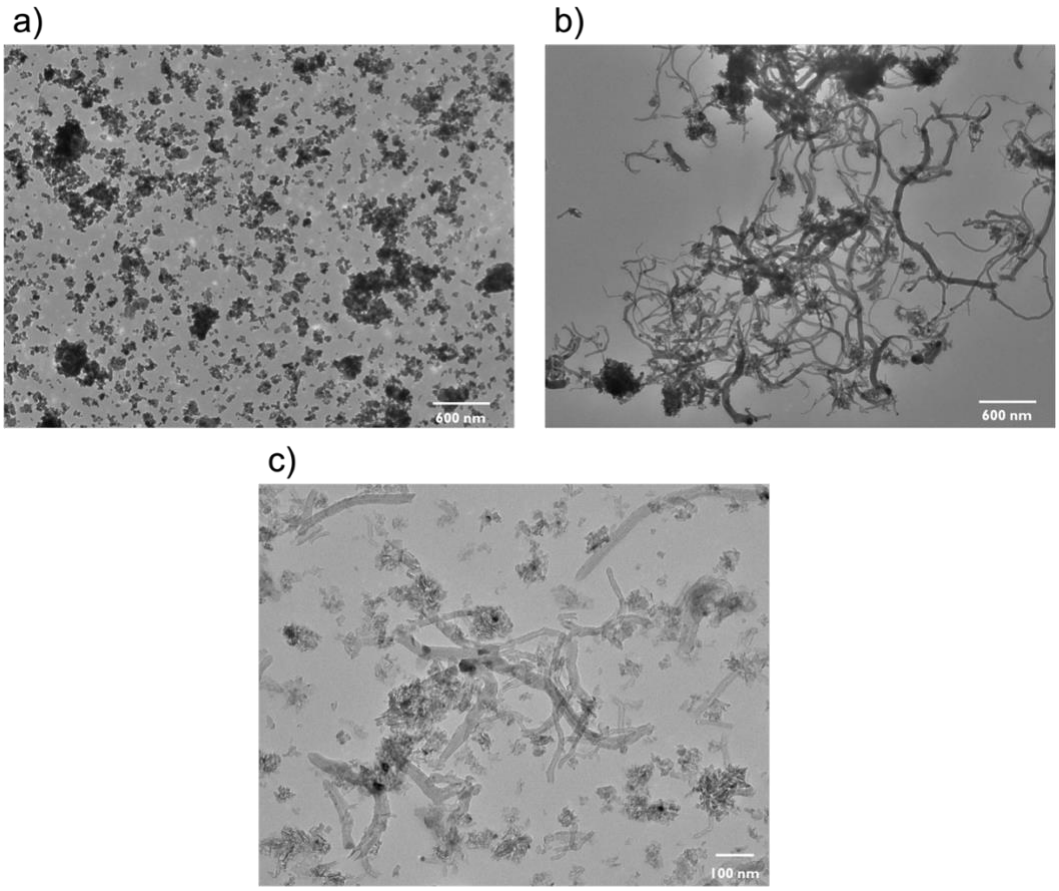

Fig.S7: TEM images show the carbon structures formed on (a) 10% Ni/MgO, (b) 10% Ni/SiO_2, and (c) 10% Ni/ γ-Al_2O_3, after reaction.

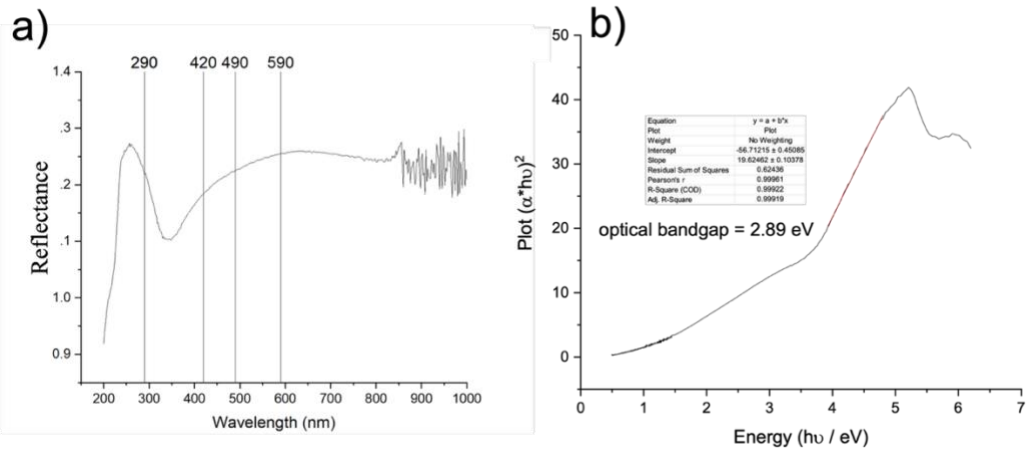

Fig. S8. Optical characterization of the fresh 10% Ni/Al_2O_3 catalyst. (a) Zoomed-in diffuse reflectance spectrum highlighting key absorption features. (b) The Tauc plot used to estimate the apparent optical band gap, indicating the material's light absorption threshold relevant for photocatalytic activity.

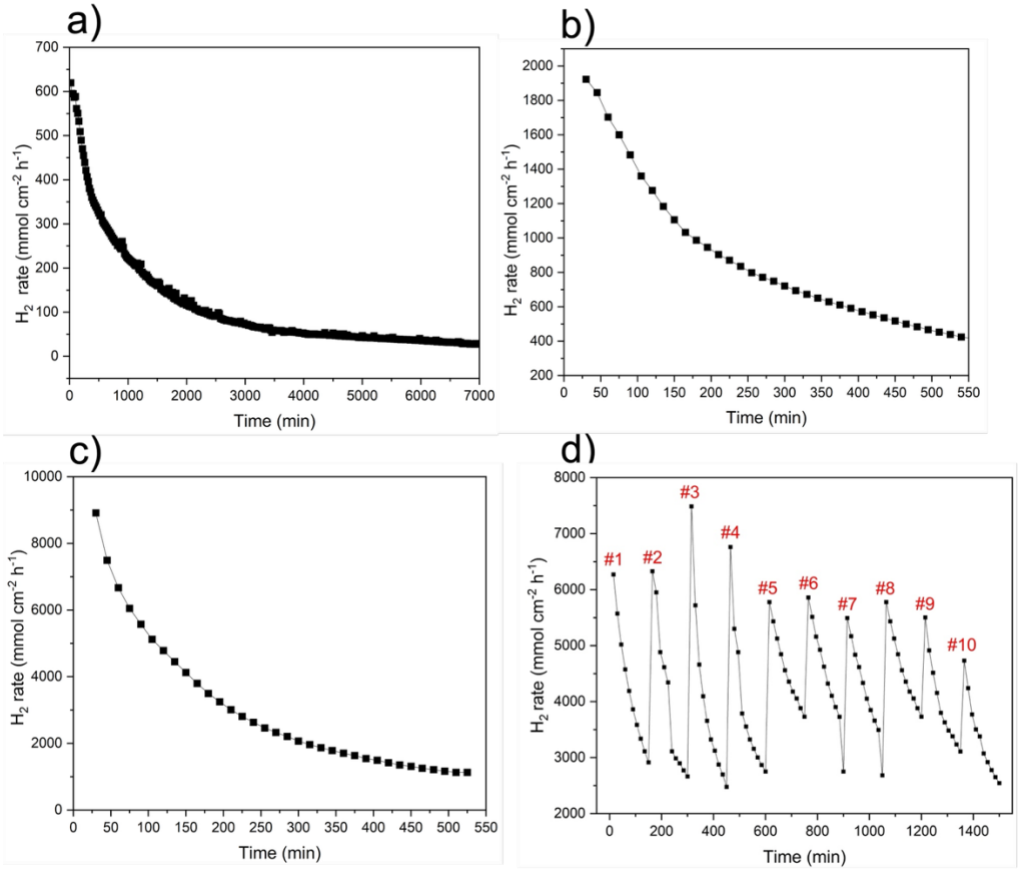

Fig. S9. Methane photolysis performance evaluation: Stability test of the 10% Ni/Al_2O_3 under a) 3.5 W cm^{-2} irradiance, b) 12 W cm^{-2} irradiance, c) 20 W cm^{-2} irradiance, d) Cycling experiments over ten cycles at 20 W cm^{-2} irradiance. Deposited carbon nanotubes from methane photolysis were removed mechanically between cycles.

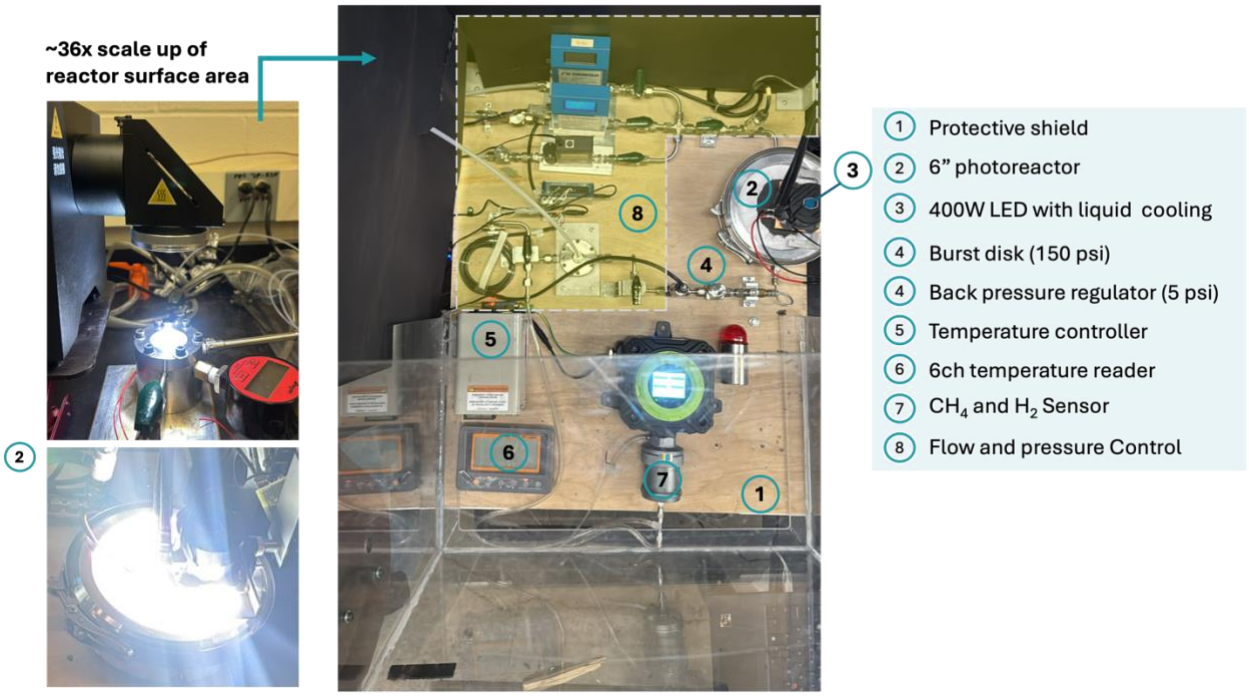

Fig. S10. Customized 36x bench scale reactor system for methane photolysis.

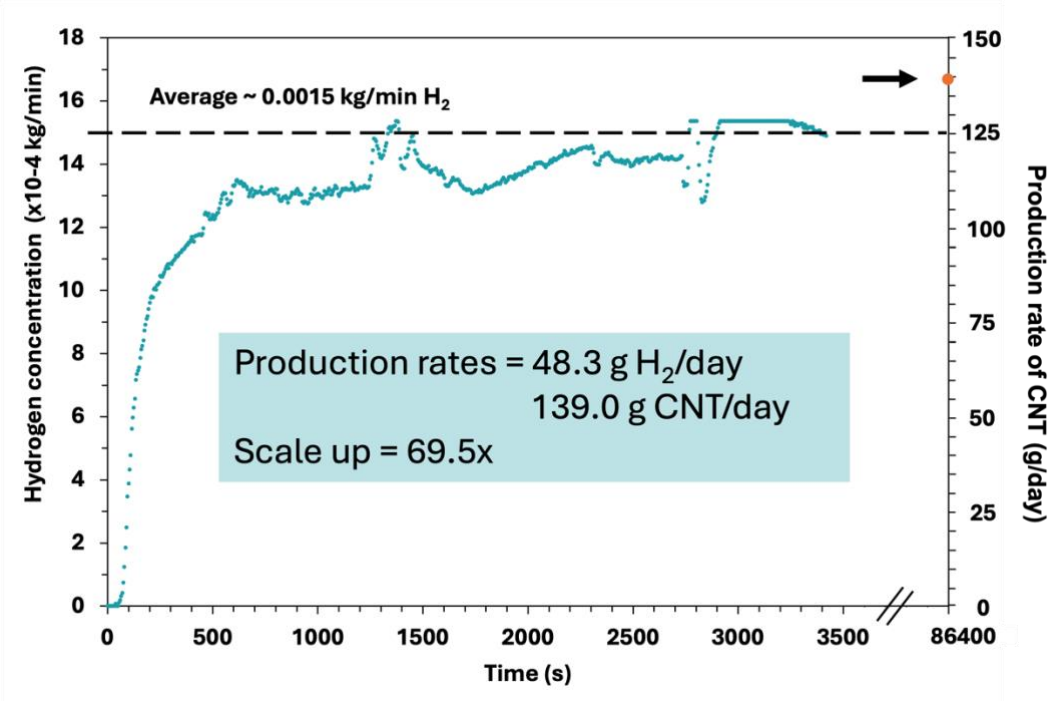

Fig. S11. H_2 and CNT projected production rate from the Customized 36x bench scale reactor system for methane photolysis.

Energy requirements calculation

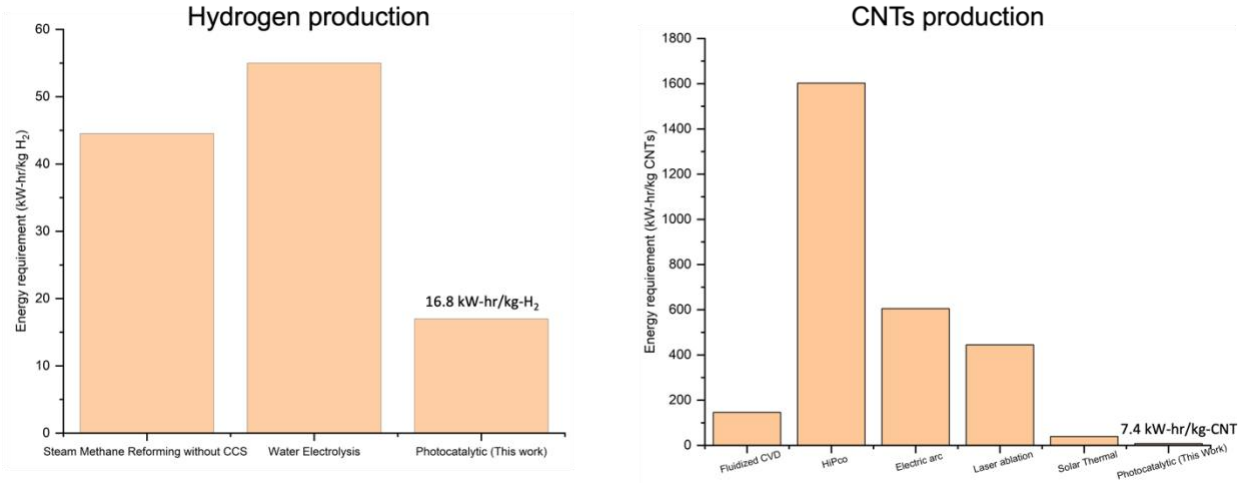

Fig. S12. H_2 and CNT energy requirements compared to other production methods[26, 27].

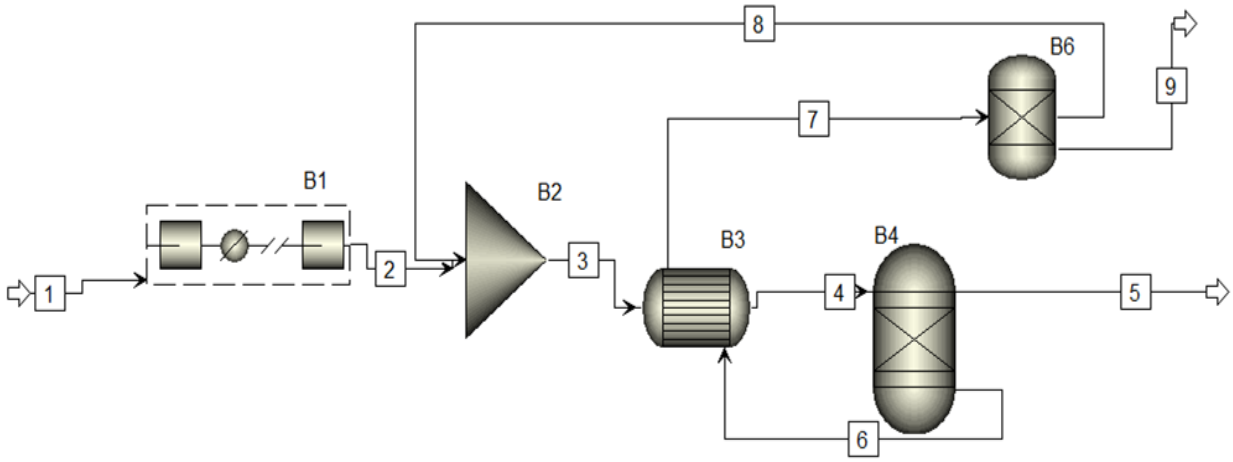

Fig. S13. Process flow diagram for the methane photolysis energy calculations.

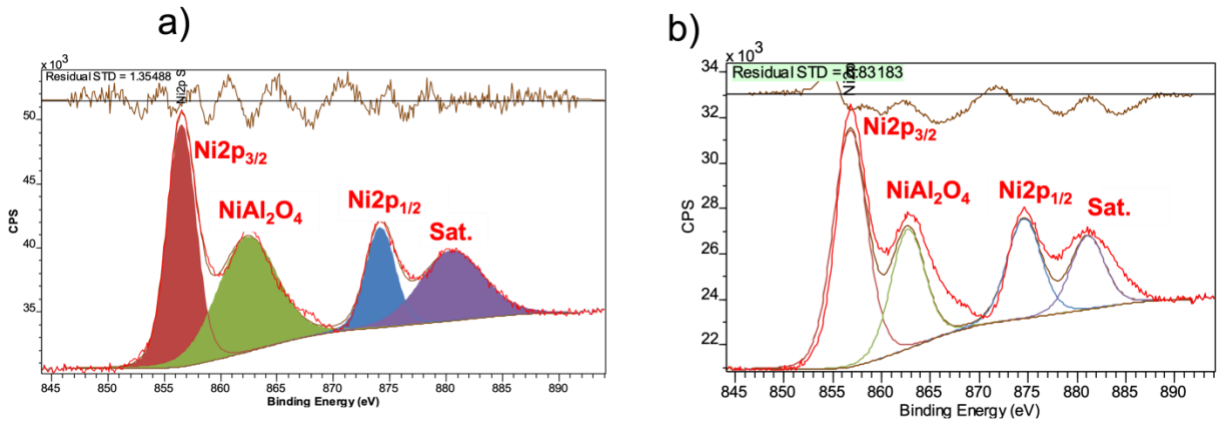

Fig. S14. Elemental and structural characterization of the pristine and the spent catalyst: Ni 2p high-resolution XPS spectrum for (a) the pristine catalyst and (b) the spent catalyst after methane photolysis at 20 W cm^{-2}.

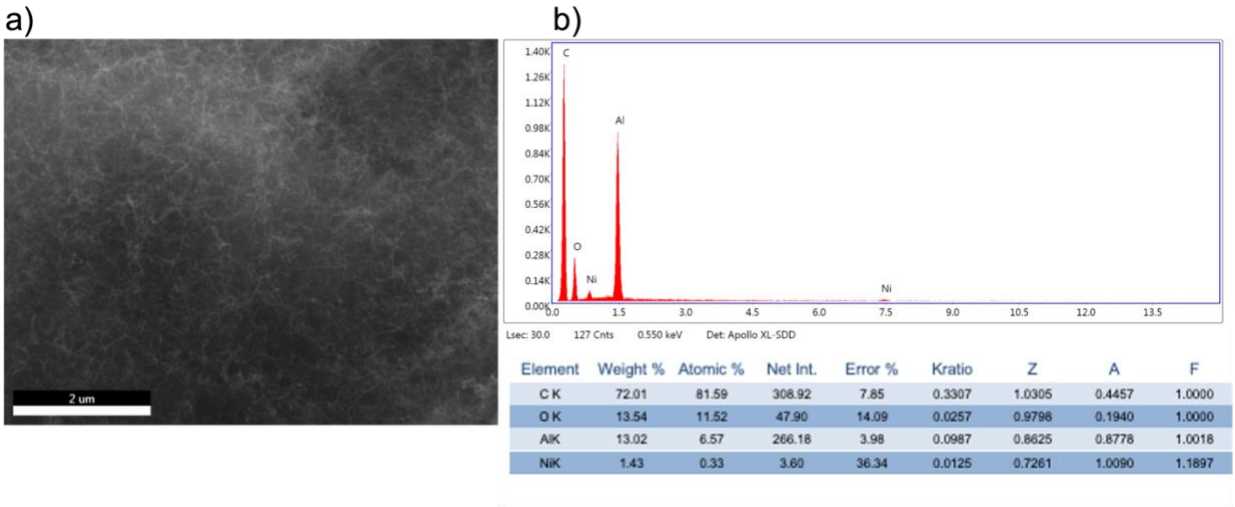

Element	Weight %	Atomic %	Net Int.	Error %	Kratio	Z	A	F
C K	72.01	81.59	308.92	7.85	0.3307	1.0305	0.4457	1.0000
O K	13.54	11.52	47.90	14.09	0.0257	0.9798	0.1940	1.0000
Al K	13.02	6.57	266.18	3.98	0.0987	0.8625	0.8778	1.0018
Ni K	1.43	0.33	3.60	36.34	0.0125	0.7261	1.0090	1.1897

Fig. S15. Morphological and elemental characterization of the separated MWCNTs: (a) SEM image of the mapped MWCNT sample and (b) corresponding EDX spectrum showing the elemental composition of the MWCNTs.

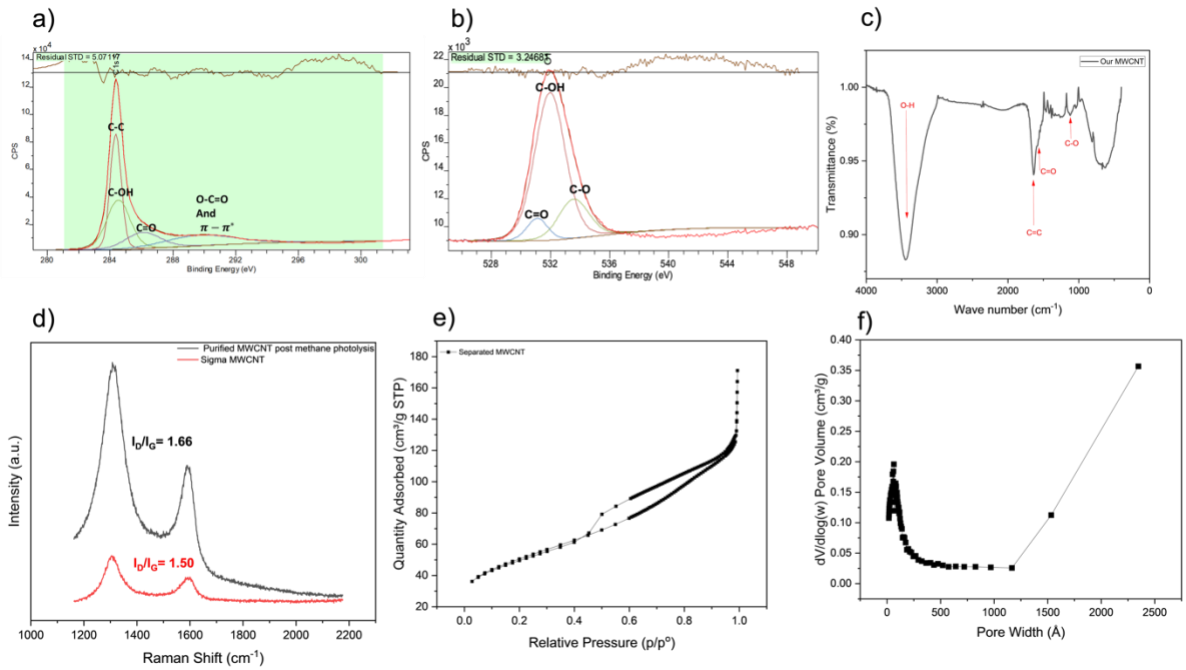

Fig. S16. Structural and elemental characterization of the mechanically separated O-MWCNT: (a) high-resolution C1s XPS spectra. (b) The high-resolution O1s XPS spectra. (c) The Fourier transform infrared (FTIR) spectra. (d) Raman spectra of the mechanically separated O-MWCNT compared to commercial Sigma MWCNT(e) N_2 adsorption-desorption isotherm. (f) pore size distribution.

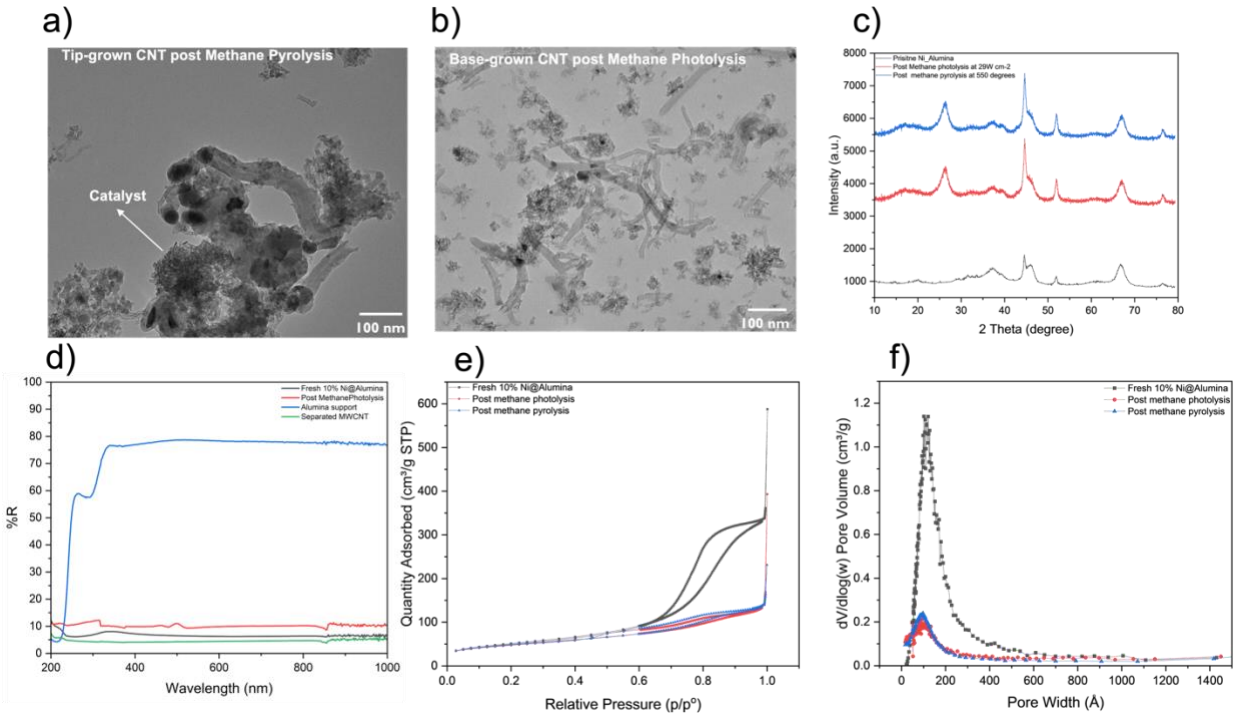

Fig. S17. Morphological and structural characterization: TEM image of (a) Tip-grown CNT post methane pyrolysis at 500 degrees and (b) base-grown CNT post methane photolysis at a light intensity of 20 W cm^{-2} ; (c) XRD of the pristine catalyst, spent catalyst post the methane photolysis, and spent catalyst post methane pyrolysis at 500 degrees; (d) reflectance spectrum of the pristine catalyst, Alumina support, separated MWCNT, the spent catalyst post methane photolysis at a light intensity of 20 W cm^{-2}**;** (e) N_2 adsorption-desorption isotherm for pristine catalyst, spent catalyst post the methane photolysis at 20 W cm^{-2}, and spent catalyst post methane pyrolysis at 500 degrees; (f) pore size distribution for the aforementioned samples.

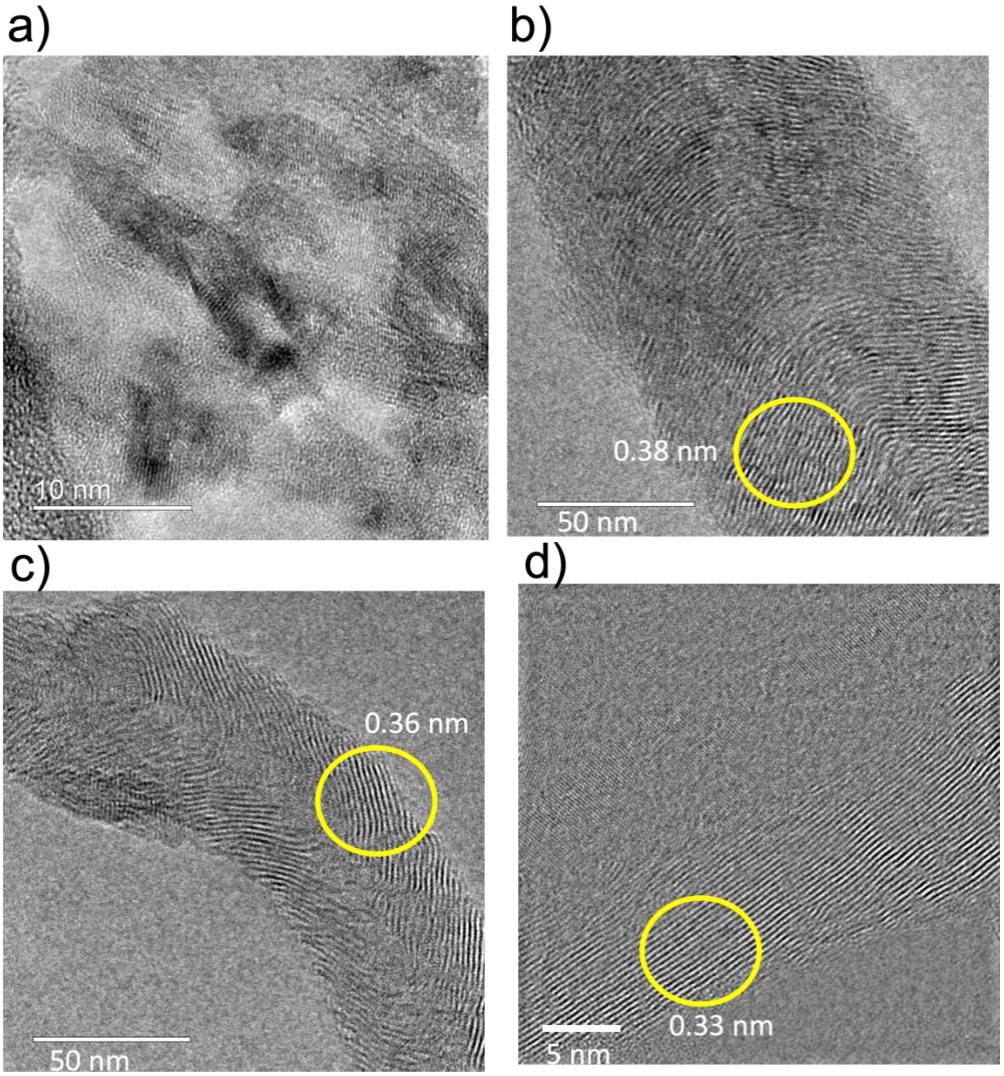

Fig. S18. Morphological characterization of the photo-grown MWCNT at different light intensity: High-resolution Transmission electron microscopy (HRTEM) image of MWCNT formed at methane Photolysis reaction, different light intensities: (a) 3 Wcm^{-2}. (b) 8 Wcm^{-2}. (c) 13 W cm^{-2} and (d) 20 W cm^{-2}.

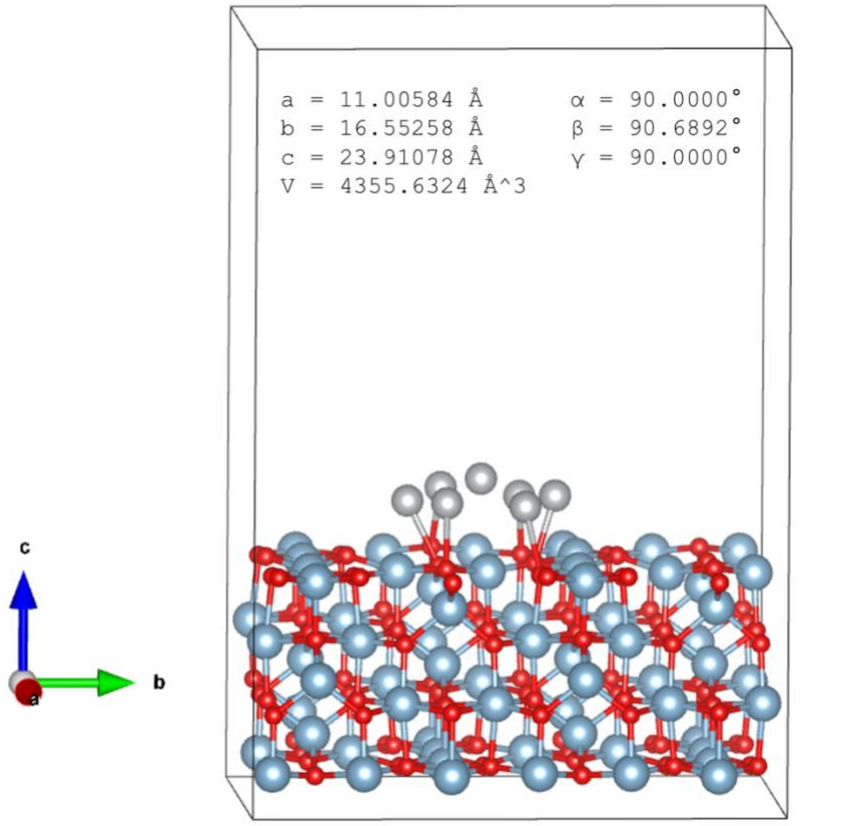

Fig. S19. DFT computational modelling of methane photolysis and CNT nucleation: Model for the relaxed Ni/γ-Al_2O_3(100) surface used for DFT simulations (blue = Al, red = O, silver = Ni), along with the corresponding cell parameters.

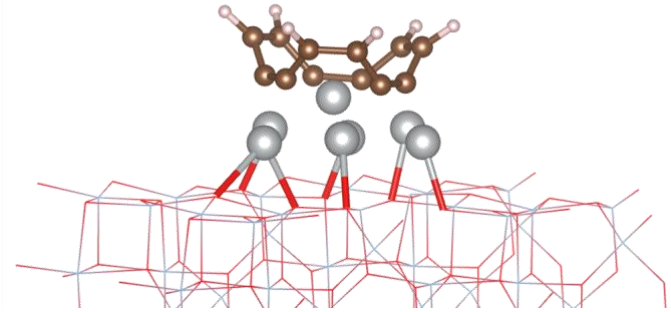

Fig. S20. DFT computational modelling of methane photolysis and CNT nucleation: Model of the 1st layer of CNT formation on the Ni/Al_2O_3 surface (silver = Ni, brown = C, white = H). Al and O atoms are omitted for clarity.

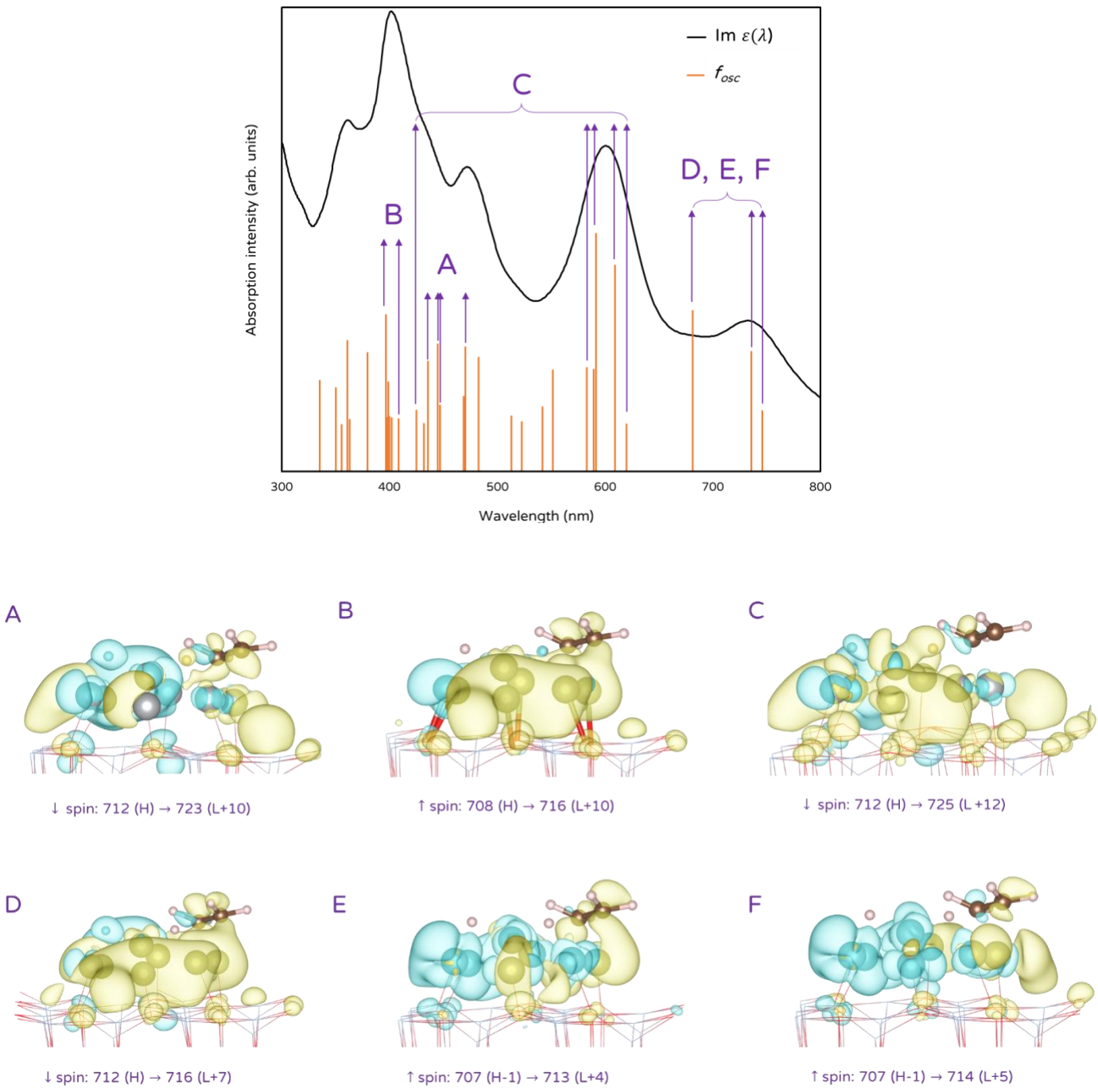

Fig. S21. DFT computational modelling of methane photolysis and CNT nucleation: Computed absorption profile of the *_(C_2H_4+2H) intermediate (structure 9 in Fig. 5), with selected excitations having the difference densities (i.e. charge density differences between a major orbital pair involved in the excitation) shown below and indicated by their corresponding letters. For the spectra, the black line corresponds to the imaginary dielectric function (sum of all directions), which simulates the absorption coefficient, and the orange lines the oscillator strengths. Difference densities are plotted at an isosurface value of 0.001 e $Bohr^{-3}$, and the yellow and blue correspond to regions of electron accumulation and depletion, respectively. H = highest occupied orbital/band, L = lowest occupied orbital/band. Al and O atoms are omitted for clarity.

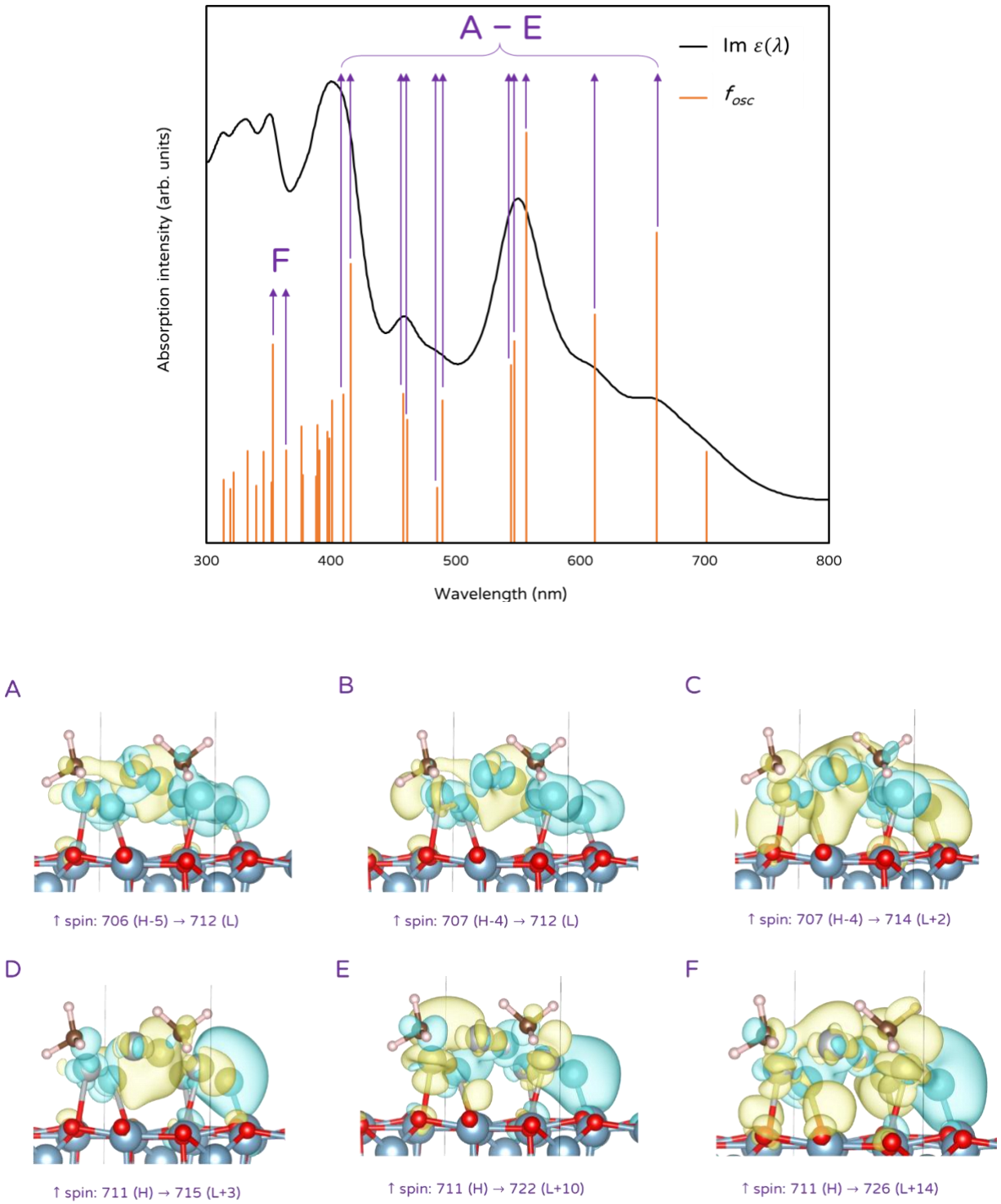

Fig. S22. DFT computational modelling of methane photolysis and CNT nucleation: Computed absorption profile of the *_($2CH_3$) intermediate (structure 6 in Fig. 5), with selected excitations having the difference densities shown below and indicated by their corresponding letters. All other parameters/descriptions are the same as those in Fig. S11, except here Al and O atoms were not omitted.

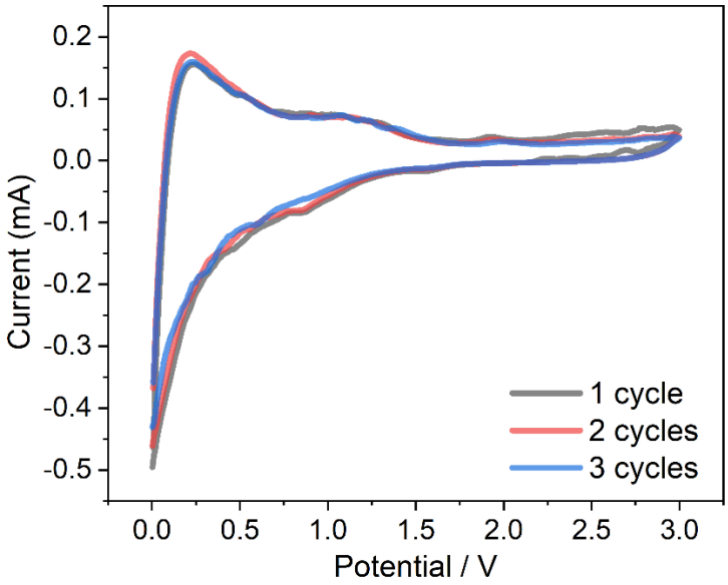

Fig. S23. Electrochemical performance of MWCNT electrode: Cyclic voltammograms of the MWCNT/Li metal electrode.

Table S1: Literature table comparing the current work to methane pyrolysis and concentrated solar methane cracking reported in the literature:

Catalyst	Reactor	Feed gas	Reaction temp (℃)	CH_4 Conversion	Turnover Frequency	H_2 selectivity	Carbon yield	Raman G/D ratio of the produced solid carbon	Ref.
10% Ni/Al_2O_3	Vertical and horizonal packed bed	100% CH_4 50% CH_4/Ar	RT using Xe lamp and white LED	10-90%	0.0238 S^{-1}	>99%	8.0 g CNT per g catalyst	1.66 for CNT separated mechanically	This work
5% Fe/Al_2O_3	Fluidized bed	100% CH_4	850	20-80%	Not reported	>99%	Not reported	1.25	[28]
Activated carbon roll	Roll-to-roll	100% CH_4	1377 ~ 3400 suns	70%	Not reported	Not reported	0.627 g	Not reported	[29]
11% Ni-Pd/CNT	Packed bed	30% CH_4/N_2	700	~55%	Not reported	Not reported	Not reported	0.66	[30]
60% Ni-Fe/SiO_2	Packed bed	30% CH_4/N_2	650	~55%	>90%	Not reported	Not reported	~1.1	[31]

70% Ni-CuZn/ Al_2O_3	Fluidized bed	100% CH_4	750	~80%	Not reported	Not reported	Not reported	1.7	[32]

We have calculated the turnover frequency (TOF), which was found to be 0.0238 s^{-1}. This indicates that each surface Ni atom facilitates one catalytic turnover approximately every 38 seconds under the applied reaction conditions.

The turnover frequency (TOF) was calculated using the following relation:

$$\text{TOF} = \frac{\text{Number of moles of } CH_4 \text{ converted per second}}{\text{Number of moles of active sites}}$$

In our case, using the data from our kinetics experiment:

Given:

- Total flow rate: 20 sccm = 20 cm^3/min
- CH_4 flow rate: 10 sccm (since it's 50% CH_4)
- Reaction time: 10 minutes
- CH_4 conversion: 8.8%

1. Calclulating the Number of moles of CH_4 converted per second:

Use the molar volume of gas at standard conditions:

1 mol gas = 24,000 cm3 at standard temp and pressure

So,

Now convert to mol/s: $\frac{10\ cm^3}{min} \times \frac{1\ mol}{24000\ cm^3} = 4.17 \times 10^{-4} \frac{mol}{min} = 6.94 \times 10^{-6} \frac{mol}{s}$

Account for CH_4 conversion (8.8%): Converted CH_4 per second $6.94 \times 10^{-6} \times 0.088 = 6.11 \times 10^{-7} \ \frac{\text{mol}}{\text{s}}$

2. The estimated **number of active catalytic sites (Ni)** in 150 mg of catalyst is:

   Ni mass: $0.10 \times 0.150 = 0.015$ g Ni

   Mo Ni: $\frac{0.015 \text{ g}}{58.69 \frac{\text{g}}{\text{mol}}} = 2.56 \times 10^{-4}$ mol of Ni

   Total number of Ni atoms: $2.56 \times 10^{-4} \times 6.022 \times 10^{23} = 1.54 \times 10^{20}$Ni atoms

   Assuming 10% dispersion, only that fraction is surface atoms:

   Active sites=$1.54 \times 10^{20} \times 0.10 = 1.54 \times 10^{19}$Ni surface atoms = $\frac{1.54 \times 10^{19}}{6.022 \times 10^{23}} = 2.56 \times 10^{-5}$ mol of active sites

TOF=$\frac{6.11 \times 10^{-7} \ \frac{\text{mol}}{\text{s}}}{2.56 \times 10^{-5} \text{ mol of active sites}}$ =0.0238 S^{-1}

Table S2: Heat Balance of the Overall Process

Stream	Mass flow (Kg/s)	Enthalpy (kJ/kg)
1	14.30	-4646.2
2	14.30	-4208.9
3	14.68	-3920.8
4	14.68	-1000.1
5	10.20	2711.8
6	4.48	14972.0
7	4.48	5392.1
8	0.38	6905.0
9	4.10	5251.5

Assumptions in Heat Balance

•System is sized to make ~6 Tons H_2 day^{-1}

•Near 100% equilibrium conversion at 1200 °C (this temperature is achievable through photocatalytic support design and minimizing thermal loss pathways at the irradiances used in this work)

•The feed to the system is pure methane at 25 °C and atmospheric pressure

•101.325 kPa and 25 °C are taken as the reference pressure and temperature

•The system operates as a steady-state process

•Kinetic and potential terms in the energy analysis can be neglected

•White LED efficiency of electricity to light energy is taken to be 65%

•The combined photothermal and photochemical efficiency of the catalyst is taken to be 50%

•The LED power density is taken as 28 W cm-2

•The irradiation area of the bed is 20 cm^2

•Compressor has an isentropic efficiency 80%

•Pressure drops are neglected

Table S3. Identification and quantification of the catalyst elements from survey scans before and after methane photolysis

Name	Binding Energy (eV)	At% Pristine catalyst	At% Spent catalyst
O 1s	532.08	45.98	38.60
C 1s	286.08	3.7	18.88
Ni 2p	857.08	0.91	0.91
Al 2p	75.08	49.36	41.62

Table S4. The texture Properties of fresh, spent metal particle catalyst and mechanically separated MWCNT extracted from Brunauer-Emmett-Teller (BET) Surface Area Analysis and Barrett-Joyner-Halenda (BJH) Pore Size and Volume Analysis.

	Pristine catalyst	Spent catalyst post methane photolysis	Spent catalyst post methane pyrolysis	Separated MWCNT post methane photolysis
BET surface area (m^2/g)	182.75	168.54	168.40	179.93
BJH average pore size (nm)	12.15	6.12	5.78	5.89
BJH pore volume (cm^3/g)	3.7E-3	9.8E-3	14.2E-3	12.2E-3

SI. Mathematical model of the process

The model follows a similar structure to the one we used in the past,[1] but pertinent modification based on the type of unit operations used are implemented.

Notation

Sets

$i \in \mathbf{I}$	Unit operations
$\mathbf{I}^{\mathrm{B}}$	Batteries
$\mathbf{I}^{\mathrm{CY}}$	Cyclones
$\mathbf{I}^{\mathrm{CM}}$	Compressors
$\mathbf{I}^{\mathrm{CSEP}}$	Catalyst regeneration units
$\mathbf{I}^{\mathrm{M}}$	Mixer units
$\mathbf{I}^{\mathrm{PSA}}$	Pressure swing adsorption units
$\mathbf{I}^{\mathrm{R}}$	Reactor units
$\mathbf{I}^{\mathrm{S}}$	Separation units
$j \in \mathbf{J}$	Streams
$\mathbf{J}_i^{\mathrm{IN}}$	Inlet stream to unit *i*
$\mathbf{J}_i^{\mathrm{OUT}}$	Outlet stream from unit *i*
$k \in \mathbf{K}$	Components
$\mathbf{K}_r^{\mathrm{REF}}$	Reference component in reaction *r*
$r \in \mathbf{R}$	Reactions
$t \in \mathbf{T}$	Time periods (years) in which the project is divided

Variables

C^{CAPITAL}	Capital investment
C^{CATALYST}	Catalyst cost
$C^{\mathrm{FEEDSTOCK}}$	Total costs of feedstocks
C^{FIXED}	Fixed costs
$C^{\mathrm{UTILITIES}}$	Total utilities cost
C^{WORKING}	Working capital
E_i	Rate of electricity consumption in unit operation *i*
E^{BATTERY}	Batteries storage capacity
F_j^{MASS}	Mass flow of stream *j*
F_j^{MOL}	Molar flow of stream *j*
$F_{j,k}^{\mathrm{MOL}}$	Molar flow of component *k* in stream *j*
F_r^{REF}	Reference component in reaction *r* occurring in unit *i*
F^{REACTOR}	Mass flow entering each of the *N* reactors modules
G_j^{CP}	Heat capacity ratio in steam j
H_j	Enthalpy of stream *j*
MSP	Minimum selling price
N	Total number of reactors
S^{REVENUE}	Total revenues
S^{CREDITS}	Total credits received from by-products

$S^{\text{DEPRECIATION}}$ Depreciation

S^{SALVAGE} Salvage value at the end of the project

TCI_i Total capital investment for unit *i*

V_j Volumetric flow rate of stream *j*

W Catalyst weight

$Y_{k,j}$ Mol fraction of component *k* in stream *j*

Parameters

α Plant capacity in terms of the total amount of CO produced [3.17 Kg/s]

$\beta^{BATTERY}$ Reference cost of batteries [414 $/kWh]

$\beta_i^{\text{C\_REF}}$ Used to estimate the total capital investment of unit *i* [$MM/(kg/s)^0.6]

Equipment	$\beta_i^{\text{C\_REF}}$
Reactor	*1*
Catalyst regeneration	*1*
PSA	*0.95*

$\beta_i^{\text{E\_REF}}$ Reference electricity consumption in unit *i* [[J/s]/[kg/s]]

Equipment	$\beta_i^{\text{E\_REF}}$
Cyclone	412.43
Catalyst regeneration	4120.34

β^{SE} Total amount total amount of energy in the form of light that reaches the reactor [108240 J/s].

γ^{CH4} Heat capacity ratio CH_4 [1.31]

γ^{H2} Heat capacity ratio H_2 [1.41]

δ^{AN} Duration of the average night [15.41 h]

δ^{LED} Cost of the LED system as a fraction of the reactor cost [2]

δ^{SPARES} Number of spares for a piece of equipment [1]

$\eta_{r,k}$ Stoichiometric coefficient of component *k* in reaction *r*

Reaction	*Component*	$\eta_{r,k}$
1	CH_4	*-1*
1	C	*1*
1	H_2	*2*

$\varepsilon_{j,k}$ Fraction of component *k* directed toward stream *j* in a separation unit

	4	5	6	7	9	10	13	14
CH_4		1	1		1			
C	0.90	0.10		1				
H_2		1	1		0.15	0.85		
CATALYST	0.9	0.1		1			0.999	0.001

$\theta_t^{\text{PERFORMANCE}}$ Factor that determines the performance of the biorefinery in period year *t*

Year	$\theta_t^{\text{PERFORMANCE}}$
Construction years 1-3	*0*
Operation year 1	*0.75*
Operation years 2-30	*1*

θ^{E} Cost of electricity [1.66e-8 $/J]

θ^{CAT2} Catalyst price [50 $/kg]

θ^{CH4} Cost of feedstock methane [0.16 $/kg]

θ^{H2} Price of hydrogen sold as byproduct [1 $/kg]

θ^{TAX} Government tax rate [21%]

$\theta_t^{\text{DEPRECIATION}}$ Depreciation factor used in time period *t*

Year	$\theta_t^{\text{DEPRECIATION}}$
Construction years 1-3	*0*
Operation year 1	*0.75*
Operation year 2	0.1429
Operation year 3	0.2449
Operation year 4	0.1749
Operation year 5	0.1249
Operation year 6	0.0893
Operation year 7	0.0892
Operation year 8	0.0893
Operation year 9	0.0446
Operation years 9-30	*0*

θ^{RATE} Internal rate of return [10%]

θ^{LANG} Factor used to determine the total capital investment for a piece of equipment [3]

λ_k^{MW} Molecular weight of component *k [Kg/mol]*

Component	λ_k^{MW}
CH_4	*0.016*
C	*0.012*
H_2	*0.002*
Catalyst	*0.101*

λ_k^{HF} Enthalpy of formation of component *k [J/mol]*

Component	λ_k^{HF}
CH_4	*-74900*
C	*900*
H_2	*0*

λ_k^{CP} Heat capacity of component *k* [J/mol-K]

Component	λ_k^{CP}
CH_4	*34.92*
C	*8.98*
H_2	*28.84*

λ^{CAT} Fraction of the catalyst removed per second [1.15e-4 1/s]

ϕ_j^{T} Temperature of stream *j*

Stream	ϕ_j^{T}
6	*308*

ϕ^{REF} Reference temperature [298.15 K]

δ Conversion [8.7 %]

δ^{H2} Maximum hydrogen mol fraction in reactor feed [20% mol/mol]

η^{B} Roundtrip battery efficiency [85 %]

η^{LED} Power conversion efficiency [32.5%]

η^{CH} Light to chemical efficiency [10%]

ϕ^{WHSV} Weight hourly space velocity [*5.67e-4* s^{-1}]

p^{PSA} Operating pressure of PSA unit [35 Bar]

p^{R} Operating pressure for the reactor [1 Bar]

r Ideal gases constant [8.314 J/K-mol]

t^{R} Temperature for the reactor [298.15 K]

Main equations in the model

We define the net present value in Eq. 1, and the required auxiliary equations for this definition in Eqs. 2-11.

$$NPV = 0 = S^{\mathrm{REVENUE}} + S^{\mathrm{CREDITS}} + S^{\mathrm{SALVAGE}} + S^{\mathrm{DEPRECIATION}} - C^{\mathrm{CAPITAL}} - C^{\mathrm{WORKING}} - C^{\mathrm{FEEDSTOCK}} - C^{\mathrm{UTILITIES}} - C^{CATALYST} - C^{\mathrm{FIXED}} \quad (1)$$

$$S^{\mathrm{REVENUE}} = MSPF_{12}^{\mathrm{MASS}} \sum_{t \in \mathbf{T}} \theta_t^{\mathrm{PERFORMANCE}} \frac{(1-\theta^{\mathrm{TAX}})}{(1+\theta^{\mathrm{RATE}})^{t-3}} \quad (2)$$

$$S^{\mathrm{CREDITS}} = \theta^{\mathrm{H2}} F_{H2}^{\mathrm{MASS}} \sum_{t \in \mathbf{T}} \theta_t^{\mathrm{PERFORMANCE}} \frac{(1-\theta^{\mathrm{TAX}})}{(1+\theta^{\mathrm{RATE}})^{t-3}} \quad (3)$$

$$S^{\text{SALVAGE}} = (0.35C^{\text{CAPITAL}} + C^{\text{WORKING}})\frac{1}{(1+\theta^{\text{RATE}})^{|\mathbf{T}|-3}} \tag{4}$$

$$S^{\text{DEPRECIATION}} = C^{\text{CAPITAL}}\sum_{t\in T}\theta_t^{\text{DEPRECIATION}}\frac{\theta^{\text{TAX}}}{(1+\theta^{\text{RATE}})^{t-3}} \tag{5}$$

$$C^{\text{CAPITAL}} = \theta^{\text{LANG}}\sum_{i\in\mathbf{I}} C_i^{\text{CAPITALINV}} \tag{6}$$

$$C^{\text{WORKING}} = 0.05C^{CAPITAL} \tag{7}$$

$$C^{\text{FEEDSTOCK}} = \sum_{t\in\mathbf{T}}\theta^{\text{CH4}}\theta_t^{\text{PERFORMANCE}}F_1^{\text{MASS}}\frac{(1-\theta^{\text{TAX}})}{(1+\theta^{\text{RATE}})^{t-3}} \tag{8}$$

$$C^{\text{UTILITIES}} = \sum_{t\in\mathbf{T}}\sum_{i\in\mathbf{I}}\theta_t^{\text{PERFORMANCE}}(\theta^{\text{E}}E_i)\frac{(1-\theta^{\text{TAX}})}{(1+\theta^{\text{RATE}})^{t-3}} \tag{9}$$

$$C^{\text{CATALYTS}} = W\sum_{t\in\mathbf{T}}\lambda^{CAT}\delta_{REACTOR}^{SPARES}\theta_t^{\text{PERFORMANCE}}\theta^{CAT2}\frac{(1-\theta^{\text{TAX}})}{(1+\theta^{\text{RATE}})^{t-3}} \tag{10}$$

$$C^{\text{FIXED}} = \sum_{t\in\mathbf{T}} 0.025C^{\text{CAPITAL}}\frac{(1-\theta^{\text{TAX}})}{(1+\theta^{\text{RATE}})^{t-3}} \tag{11}$$

We also define the total molar flow of each stream (Eq. 11), the total mass flow (Eq. 12), the stream enthalpy (Eq. 13), and the molar flow of components (Eq. 14)

$$F_j^{\text{MOL}} = \sum_{k\in\mathbf{K}} F_{j,k}^{\text{MOL}}, \forall j \in \mathbf{J} \tag{11}$$

$$F_j^{\text{MASS}} = \sum_{k\in\mathbf{K}} \lambda_k^{\text{MW}}F_{j,k}^{\text{MOL}}, \forall j \in \mathbf{J} \tag{12}$$

$$H_j = \sum_{k\in\mathbf{K}}(\lambda_k^{\text{HF}} + \lambda_k^{\text{CP}}(\phi_j^{\text{T}} - \phi^{\text{REF}}))F_{j,k}^{\text{MOL}}, \forall j \in \left(\mathbf{J}_i^{\text{IN}} \vee \mathbf{J}_i^{\text{OUT}}\right), i \in \mathbf{I} \tag{13}$$

$$Y_{k,j} = \frac{F_{j,k}^{MOL}}{F^{MOL}} \forall k \in \mathbf{K}, j \in \left(\mathbf{J}_i^{IN} \cup \mathbf{J}_i^{OUT}\right), i \in \mathbf{I}^{CM} \tag{14}$$

The plant capacity is constrained by Eq. 15:

$$F_{10,H2}^{MOL}\delta_{H2}^{MW} = \alpha \tag{15}$$

Three different types of mass balances are written (1) for the inlet mixer and the compressors (Eq. 16) (2) for the reactor (Eqs. 17-18) and (2) for the separation units (cyclone, PSA, and catalyst regeneration) (Eq. 19).

$$\sum_{j\in\mathbf{J}_i^{\text{IN}}} F_{j,k}^{\text{MOL}} = \sum_{j\in\mathbf{J}_i^{\text{OUT}}} F_{j,k}^{\text{MOL}}, \forall k \in \mathbf{K}, i \in (\mathbf{I}^{\boldsymbol{M}} \cup \mathbf{I}^{\boldsymbol{CM}}) \tag{16}$$

$$F_{j,k}^{\text{MOL}} = \varepsilon_{j,k}\left[\sum_{j'\in\mathbf{J}_i^{\text{IN}}} F_{j',k}^{\text{MOL}} + \sum_{r\in\mathbf{R}}\delta\eta_{k,r}F_r^{\text{REF}}\right], \forall j \in \mathbf{J}_i^{\text{OUT}}, k \in \mathbf{K}, i \in \mathbf{I}^{\text{R}} \tag{17}$$

$$F_{r,i}^{\mathrm{REF}} = \sum_{k \in \mathbf{K}_r^{\mathrm{REF}}} \sum_{j \in \mathbf{J}_i^{\mathrm{IN}}} F_{j,k}^{\mathrm{MOL}}, \forall r \in \mathbf{R}, i \in \mathbf{I}^{\mathrm{R}} \tag{18}$$

$$F_{j,k}^{\mathrm{MOL}} = \varepsilon_{j,k} \sum_{j' \in \mathbf{J}_i^{\mathrm{IN}}} F_{j',k}^{\mathrm{MOL}}, \forall k \in \mathbf{K}, j \in \mathbf{J}_i^{\mathrm{OUT}}, i \in \mathbf{I}^{\mathrm{CY}} \cup \mathbf{I}^{\mathrm{PSA}} \cup \mathbf{I}^{\mathrm{CSEP}} \tag{19}$$

The capital cost for the reactor (Eqs. 20-22) and battery system (Eqs. 23-24) are established following the same approach described in Viasus Perez et al, 2023.[1] The reference cost for the reactor in Eq. 20 is guessed following the approach described in the main text. Cyclone (25-26) and compressor (27-29) costs are estimated using known cost correlations. For the PSA unit and the catalyst recovery system we use the sixth-then rule for scaling, using reference costs for equipment obtained in the literature (PSA unit), or assumed values based on a reasonable guess (catalyst recovery) (Eq. 30).

$$TCI_i = (1+\delta^{\mathrm{LED}})\gamma_i N \left(\frac{F^{\mathrm{REACTOR}}}{\beta_i^{\mathrm{C\_REF}}} \right)^{0.6}, \forall i \in \mathbf{I}^{\mathrm{R}} \tag{20}$$

$$N = \frac{\sum_{j \in \mathbf{J}_i^{\mathrm{OUT}}} H_j - \sum_{j \in \mathbf{J}_i^{\mathrm{IN}}} H_j}{\beta^{\mathrm{SE}} \eta^{\mathrm{CH}}} \tag{21}$$

$$F^{REACTOR} = \frac{\sum_{j \in \mathbf{J}_i^{\mathrm{IN}}} F_j^{\mathrm{MASS}}}{N} \tag{22}$$

$$TCI_i = \beta^{BATTERY} E^{BATTERY}, \forall i \in \mathbf{I}^{\mathrm{B}} \tag{23}$$

$$E^{BATTERY} = \frac{\delta^{AN}}{\eta^{LED}\eta^{CH}\eta^{B}} \left(\sum_{j \in \mathbf{J}_i^{\mathrm{OUT}}} H_j - \sum_{j \in \mathbf{J}_i^{\mathrm{IN}}} H_j \right), \forall i \in \mathbf{I}^{\mathrm{R}} \tag{24}$$

$$TCI_i = 2.12 e^{9.3485 - 0.7892 \log(2118.882 V_5) + 0.08487 \log(2118.882 V_5)^2}, \quad \forall\, i \in \mathbf{I}^{\mathrm{CY}} \tag{25}$$

$$V_5 = \frac{\left(F_{5,CH4}^{MOL} + F_{5,H2}^{MOL}\right) r t^R}{p^R} \tag{26}$$

$$TCI_i = 1.9968 e^{9.1553 + 0.63 \log(0.001341022909 E_i)}, \forall\, i \in \mathbf{I}^{\mathrm{CM}} \tag{27}$$

$$E_i = \sum_{j \in \mathbf{J}_i^{\mathrm{IN}}} \left(cp_{CH4} F_{j,CH4}^{MOL} + cp_{H2} F_{j,H2}^{MOL} \right) \phi_j^{\mathrm{T}} \left(\frac{p^{PSA}}{p^R} \right)^{\left[\frac{\left(G_j^{CP} - 1\right)}{G_j^{CP}} - 1 \right]}, \forall\, i \in \mathbf{I}^{\mathrm{CM}} \tag{28}$$

$$\frac{1}{\sum_{j \in \mathbf{J}_i^{\mathrm{IN}}} G_j^{CP} - 1} = \sum_{j \in \mathbf{J}_i^{\mathrm{IN}}} \frac{Y_{j,CH4}}{\gamma^{CH4}} + \frac{1 - Y_{j,H2}}{\gamma^{H2}}, , \forall\, i \in \mathbf{I}^{\mathrm{CY}} \tag{29}$$

$$TCI_i = \beta_i^{\mathrm{C\_REF}} \left(\frac{F_j^{\mathrm{MASS}}}{\beta_i^{\mathrm{FM\_REF}}} \right)^{0.6}, \forall i \in (\mathbf{I}^{\mathrm{PSA}} \cup \mathbf{I}^{\mathrm{CSEP}}) \tag{30}$$

We estimate the electricity consumption (most relevant utility and only one considered in this work) in different units: reactor (Eq. 32), cyclone and catalyst regeneration (Eq. 33), and compressor (Eq. 28).

$$E_i = \left(\frac{(\delta^{AN}/24)}{\eta^{LED}\eta^{CH}} + \frac{1-(\delta^{AN}/24)}{\eta^{LED}\eta^{CH}\eta^{B}}\right)\left(\sum_{j\in \mathbf{J}_i^{\mathrm{OUT}}} H_j - \sum_{j\in \mathbf{J}_i^{\mathrm{IN}}} H_j\right), \forall i \in \mathbf{I}^{\mathrm{R}} \quad (32)$$

$$E_i = \beta_i^{\mathrm{E\_REF}} \sum_{j\in \mathbf{J}_i^{\mathrm{IN}}} \frac{F_j^{MASS}}{\beta_i^{FM\_REF}}, \forall i \in \mathbf{I}^{\mathbf{CY}\cup\mathbf{I}^{\mathrm{CSEP}}} \quad (33)$$

The catalyst consumption in Eq. 34.

$$W = \frac{F_{2,CH4}^{MOL}\lambda_k^{\mathrm{MW}}}{\phi^{WHSV}} \quad (34)$$

Finally, we constraint the composition of the reactor inlet such that it is below a preestablished threshold (Eq. 35).

$$F_{2,H2} \leq \delta^{H2} F_2^{MOL} \quad (35)$$

SI. Sensitivity analysis of MSP of MWCNT with respect to the price of hydrogen

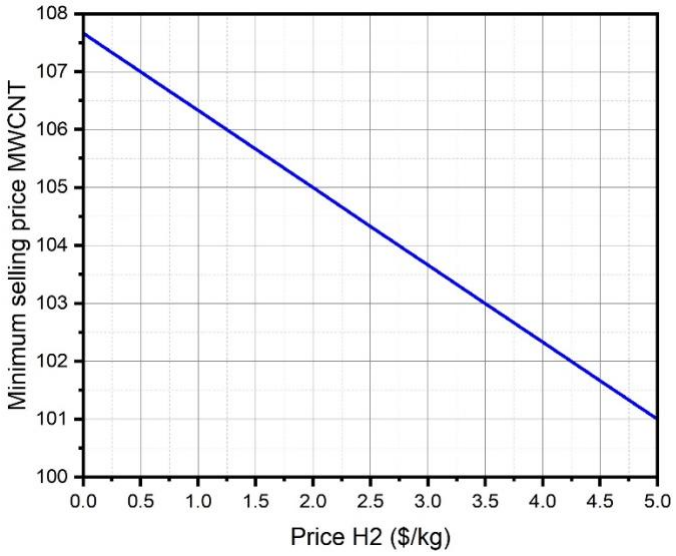

Figure S24. Sensitivity analysis showing the effect of H2 price on the MSP of MWCNT.

SI. Lifecycle inventory

Table S5. Preliminary inventory for lifecycle analysis

	S1	**S2**	**S3**	**S4**
Methane consumption [MJ/s]	7037.4	7037.4	7037.4	7037.4
Electricity [MJ/s]	2065.2	332.0	2065.2	332.0
C captured [kg/s]	-8.7175	-31.383	-8.7175	-31.383

C emitted [kg/s]	26.1525	3.487	26.1525	3.487
H_2 production [MJ/s]	3803.6196	3803.6196	3803.6196	3803.6196

References

1. J. C. Maxwell, *A treatise on electricity and magnetism*, Oxford: Clarendon Press, 1873.
2. K. Pietrak and T. S. Wiśniewski, *Journal of Power Technologies*, 2014, 14-24%V 95.
3. L. A. Glasgow, *Transport phenomena: an introduction to advanced topics*, John Wiley & Sons, 2010.
4. M. Soomro and R. Hughes, *The Canadian Journal of Chemical Engineering*, 1979, **57**, 24-28.
5. G. Baffou, P. Berto, E. Bermúdez Ureña, R. Quidant, S. Monneret, J. Polleux and H. Rigneault, *ACS Nano*, 2013, **7**, 6478-6488.
6. Y. Dubi, I. W. Un and Y. Sivan, *Chemical Science*, 2020, **11**, 5017-5027.
7. G. Kresse and J. Hafner, *Physical Review B*, 1993, **47**, 558-561.
8. G. Kresse and J. Hafner, *Physical Review B*, 1994, **49**, 14251-14269.
9. G. Kresse and J. Furthmüller, *Computational Materials Science*, 1996, **6**, 15-50.
10. G. Kresse and J. Furthmüller, *Physical Review B*, 1996, **54**, 11169-11186.
11. G. Kresse and D. Joubert, *Physical Review B*, 1999, **59**, 1758-1775.
12. J. Ning, M. Kothakonda, J. W. Furness, A. D. Kaplan, S. Ehlert, J. G. Brandenburg, J. P. Perdew and J. Sun, *Physical Review B*, 2022, **106**, 075422.
13. M. Kothakonda, A. D. Kaplan, E. B. Isaacs, C. J. Bartel, J. W. Furness, J. Ning, C. Wolverton, J. P. Perdew and J. Sun, *ACS Materials Au*, 2023, **3**, 102-111.
14. M. Digne, P. Sautet, P. Raybaud, P. Euzen and H. Toulhoat, *Journal of Catalysis*, 2004, **226**, 54-68.
15. X. Krokidis, P. Raybaud, A.-E. Gobichon, B. Rebours, P. Euzen and H. Toulhoat, *The Journal of Physical Chemistry B*, 2001, **105**, 5121-5130.
16. T. Björkman, *Computer Physics Communications*, 2011, **182**, 1183-1186.
17. M. Gajdoš, K. Hummer, G. Kresse, J. Furthmüller and F. Bechstedt, *Physical Review B*, 2006, **73**, 045112.
18. S. Albrecht, L. Reining, R. Del Sole and G. Onida, *Physical Review Letters*, 1998, **80**, 4510-4513.
19. M. Rohlfing and S. G. Louie, *Physical Review Letters*, 1998, **81**, 2312-2315.
20. J. Heyd, G. E. Scuseria and M. Ernzerhof, *The Journal of Chemical Physics*, 2003, **118**, 8207-8215.
21. S. Grimme, J. Antony, S. Ehrlich and H. Krieg, *The Journal of Chemical Physics*, 2010, **132**.
22. S. Grimme, S. Ehrlich and L. Goerigk, *Journal of Computational Chemistry*, 2011, **32**, 1456-1465.
23. M. Bokdam, J. Lahnsteiner, B. Ramberger, T. Schäfer and G. Kresse, *Physical Review Letters*, 2017, **119**, 145501.
24. V. Wang, N. Xu, J.-C. Liu, G. Tang and W.-T. Geng, *Computer Physics Communications*, 2021, **267**, 108033.
25. K. Momma and F. Izumi, *Journal of applied crystallography*, 2011, **44**, 1272-1276.
26. D. Kushnir and B. A. Sandén, *Journal of Industrial Ecology*, 2008, **12**, 360-375.
27. H2A: Hydrogen Analysis Production Models, https://www2.nrel.gov/hydrogen/h2a-production-models, (accessed April 12, 2025).
28. E. Sun, S. Zhai, D. Kim, M. Gigantino, V. Haribal, O. S. Dewey, S. M. Williams, G. Wan, A. Nelson, S. Marin-Quiros, J. Martis, C. Zhou, J. Oh, R. Randall, M. Kessler, D. Kong, J. Rojas, A. Tong, X. Xu, C. Huff, M. Pasquali, R. Gupta, M. Cargnello and A. Majumdar, *Cell Reports Physical Science*, 2023, **4**.

29. M. Abuseada, C. Wei, R. M. Spearrin and T. S. Fisher, *Energy & Fuels*, 2022, **36**, 3920-3928.
30. I. W. Wang, R. A. Dagle, T. S. Khan, J. A. Lopez-Ruiz, L. Kovarik, Y. Jiang, M. Xu, Y. Wang, C. Jiang, S. D. Davidson, P. Tavadze, L. Li and J. Hu, *Catalysis Science & Technology*, 2021, **11**, 4911-4921.
31. D. Ayillath Kutteri, I. W. Wang, A. Samanta, L. Li and J. Hu, *Catalysis Science & Technology*, 2018, **8**, 858-869.
32. K. R. Parmar, K. K. Pant and S. Roy, *Energy Conversion and Management*, 2021, **232**, 113893.